

The interaction of planets with a disc with MHD turbulence III: Flow morphology and conditions for gap formation in local and global simulations

John C.B. Papaloizou, Richard P. Nelson & Mark D. Snellgrove

Astronomy Unit, Queen Mary, University of London, Mile End Rd, London E1 4NS

Received/Accepted

ABSTRACT

We present the results of both global cylindrical disc simulations and local shearing box simulations of protoplanets interacting with a disc undergoing MHD turbulence with zero net flux magnetic fields. We investigate the nature of the disc response and conditions for gap formation. This issue is an important one for determining the type and nature of the migration of the protoplanet, with the presence of a deep gap being believed to enable slower migration.

For both types of simulation we find a common pattern of behaviour for which the main parameter determining the nature of the response is $M_p R^3 / (M_* H^3)$, with M_p , M_* , R , and H being the protoplanet mass, the central mass, the orbital radius and the disc semi-thickness respectively. We find that as $M_p R^3 / (M_* H^3)$ is increased to ~ 0.1 the presence of the protoplanet is first indicated by the appearance of the well known trailing wake which, although it may appear to be erratic on account of the turbulence, appears to be well defined. Once $M_p R^3 / (M_* H^3)$ exceeds a number around unity a gap starts to develop inside which the magnetic energy density tends to be concentrated in the high density wakes. This condition for gap formation can be understood from simple dimensional considerations of the conditions for nonlinearity and the balance of angular momentum transport due to Maxwell and Reynolds' stresses with that due to tidal torques applied to the parameters of our simulations.

An important result is that the basic flow morphology in the vicinity of the protoplanet is very similar in both the local and global simulations. This indicates that, regardless of potentially unwanted effects arising from the periodic boundary conditions, local shearing box simulations, which are computationally less demanding, capture much of the physics of disc–planet interactions. Thus they may provide a useful tool for studying the local interaction between forming protoplanets and turbulent, protostellar discs.

Key words: accretion, accretion disks — MHD, instabilities, turbulence – planetary systems: formation, protoplanetary discs

1 INTRODUCTION

The recent and ongoing discovery of extrasolar giant planets has stimulated much current investigation of theories of planet formation (e.g. Mayor & Queloz 1995; Marcy, Cochran, & Mayor 1999; Vogt et al. 2002). At the present time giant planets are believed to originate in protostellar discs. Possible formation scenarios are either through direct gravitational fragmentation of a young protostellar disc (e.g. Boss 2001) or through the accumulation of a solid core which then undergoes mass build up through gas accretion once the core mass reaches $\simeq 15$ Earth masses (e.g. Bodenheimer & Pollack 1986; Pollack et al. 1996). In either scenario giant

planets are likely to form at significantly larger radii than those observed, requiring a migration mechanism to bring them closer to the central star. Disc–protoplanet interaction provides a natural mechanism.

In the standard picture a protoplanet exerts torques on a protostellar disc through the excitation of spiral density waves (e.g. Goldreich & Tremaine 1979). These waves carry an associated angular momentum flux which is deposited in the disc where the waves are damped. This process results in a negative torque acting on the protoplanet from the outer disc and a positive torque acting on it from the disc interior to its orbit.

Previous work on the interaction between a protoplanet

and a laminar disc with Navier Stokes viscosity (Papaloizou & Lin 1984; Lin & Papaloizou 1993) indicates that a sufficiently massive protoplanet can open up an annular gap in the disc centred on its orbital radius. For typical protostellar disc models the protoplanet needs to be approximately a Jovian mass for gap formation to occur. Recent simulations (Bryden et al. 1999; Kley 1999; Lubow, Seibert, & Artymowicz 1999; D'Angelo, Henning, & Kley 2002) examined the formation of gaps by giant protoplanets, and also estimated the maximal gas accretion rate onto them. The orbital evolution of a Jovian mass protoplanet embedded in a standard laminar viscous protostellar disc model was studied by Nelson et al. (2000). They found that that gap formation and accretion of the inner disc by the central mass led to the formation of a low density inner cavity in which the planet orbits. Interaction with the outer disc resulted in inward type II migration on a time scale of a few $\times 10^5$ yr. The disc models in these studies all adopted an anomalous disc viscosity modelled through the Navier–Stokes equations without consideration of its origin.

The most likely origin of the viscosity is through MHD turbulence resulting from the magnetorotational instability (MRI) (Balbus & Hawley 1991) and it has recently become possible through improvements in computational resources to simulate discs in which this underlying mechanism responsible for angular momentum transport is explicitly calculated. This is necessary because the turbulent fluctuations do not necessarily result in transport phenomena that can be modelled with the Navier Stokes equation.

To this end Papaloizou & Nelson (2003) and Nelson & Papaloizou (2003a) (hereafter papers I and II) developed models of turbulent protostellar accretion discs and considered the interaction with a giant protoplanet of 5 Jupiter masses. The large mass was chosen to increase the scale of the interaction so reducing the computational resources required. This protoplanet was massive enough to maintain a deep gap separating the inner and outer disc and exert torques characteristic of type II migration.

It is the purpose of this paper to extend our previous work to a wider range of protoplanetary masses and disc parameters. In particular we study the nature of the disc–protoplanet interaction as the protoplanet mass increases and investigate the condition for gap formation.

To do this we utilise both global and local simulations. The global simulations are more realistic but too computationally demanding for significant extended parameter surveys. On the other hand local shearing box simulations being less computationally demanding enable a wider parameter survey at higher resolution. Of course because of the high degree of symmetry they do not allow migration rates to be estimated but most other features of the global simulations are reproduced.

In this paper we focus on the morphology of the disc response as a function of the protoplanet mass leaving the analysis of the disc–protoplanet torques resulting from the interaction to a companion paper (Nelson & Papaloizou 2003b – hereafter paper IV).

The plan of this paper is as follows:

In §2 we describe both the initial global disc models and the shearing box models used for the simulations.

In §3 we discuss the nature of the waves that can propagate and how their excitation leads to the existence of the

prominent wake that is frequently seen in the simulations of protoplanet disc interaction even when the disc is turbulent. In §4 we describe the numerical procedure used. In §5 we present the results of the local and global simulations. Finally, we summarize our results in §6.

2 SET UP OF INITIAL MODELS

In this paper we have performed both global and local simulations of protoplanets interacting with model discs in which MHD turbulence driven by the MRI operates. We consider simulations for which the magnetic field has zero net flux and therefore an internally generated dynamo is maintained. We determine the disc response as a function of the protoplanet mass and as far as is possible study its characteristics for the different kinds of model focusing on the conditions that determine whether the response is weak (linear) or strong (non linear). We now describe the model set up for the global and local simulations.

2.1 Global Simulations

The governing equations for MHD written in a frame rotating with arbitrary uniform angular velocity $\Omega_p \hat{\mathbf{k}}$ with $\hat{\mathbf{k}}$ being the unit vector along the rotation axis assumed to be in the vertical (z) direction are the continuity equation:

$$\frac{\partial \rho}{\partial t} + \nabla \cdot \rho \mathbf{v} = 0, \quad (1)$$

the equation of motion

$$\frac{\partial \mathbf{v}}{\partial t} + \mathbf{v} \cdot \nabla \mathbf{v} + 2\Omega_p \hat{\mathbf{k}} \times \mathbf{v} = -\frac{\nabla p}{\rho} - \nabla \Phi + \frac{(\nabla \times \mathbf{B}) \times \mathbf{B}}{4\pi\rho}, \quad (2)$$

and the induction equation

$$\frac{\partial \mathbf{B}}{\partial t} = \nabla \times (\mathbf{v} \times \mathbf{B}). \quad (3)$$

where \mathbf{v} , P , ρ , \mathbf{B} and Φ denote the fluid velocity, pressure, density and magnetic field respectively. The potential $\Phi = \Phi_{rot} + \Phi_G$ contains contributions due to gravity, Φ_G and the centrifugal potential $\Phi_{rot} = -(1/2)\Omega_p^2 |\hat{\mathbf{k}} \times \mathbf{r}|^2$.

The gravitational contribution is taken to be due to a central mass M_* and planet with mass M_p . Thus in cylindrical coordinates (r, ϕ, z) with the planet located at $(r_p, \phi_p, 0)$ and the star located at $(r_*, \phi_*, 0)$ $\Phi_G = \Phi_c + \Phi_p$, where

$$\Phi_c = -\frac{GM_*}{|\mathbf{r} - \mathbf{r}_*|} \quad \text{and} \quad \Phi_p = -\frac{GM_p}{\sqrt{r^2 + r_p^2 - 2rr_p \cos(\phi - \phi_p) + b^2}}. \quad (4)$$

Here, as in papers I and II, for reasons of computational expediency, we have neglected the dependence of the gravitational potentials on z along with the vertical stratification of the disc. Thus the global simulations are of cylindrical discs (e.g. Armitage 1998, 2001; Hawley 2000, 2001; Steinacker & Papaloizou 2002). To model the effects of the reduction of the planet potential with vertical height, we have incorporated a softening length b in its potential.

We use a locally isothermal equation of state in the form

$$P = \rho \cdot c(r)^2, \quad (5)$$

with c denoting the sound speed which is specified as a fixed function of the cylindrical radius r . The above gives the basic equations used for the global simulations.

2.1.1 Initial and Boundary Conditions

The global simulations presented here all use the same underlying turbulent disc model. This model has a constant aspect ratio $H/r \equiv c(r)/(r\Omega) = 0.07$, where Ω is the disc angular velocity as measured in the inertial frame. The inner radial boundary of the computational domain is at $R_{in} = 1$ and the outer boundary is at $R_{out} = 8$. The boundary conditions employed are very similar to those described in paper I. Regions of the disc in the close vicinity of the inner and outer boundaries were given non-Keplerian angular velocity profiles that are stable to the MRI, and which have large values of the density in order to maintain radial hydrostatic equilibrium. These regions act as buffer zones that prevent the penetration of magnetic field to the radial boundaries, thus maintaining zero-net flux in the computational domain. The inner buffer zone runs from $r = 1.14$ to $r = R_{in}$, and the outer buffer zone runs from $r = 7.0$ to $r = R_{out}$.

The disc was initiated with a zero net flux toroidal magnetic field in a finite annulus in the disc between the radii $2 \leq r \leq 6$. The initial disc model had azimuthal domain running between $\phi = 0$ to $\pi/4$, and vertical domain from $z_{min} = -0.21$ to $z_{max} = 0.21$. Periodic boundary conditions were employed in the vertical and azimuthal directions.

The unperturbed disc model was evolved until the MRI produced a turbulent disc model with a statistically steady turbulence. This model had a volume averaged value of the ratio of magnetic energy to mean pressure of $\simeq 0.011$ and a volume averaged value of the Shakura–Sunyaev stress parameter $\alpha \simeq 7 \times 10^{-3}$. In order to generate the full 2π disc models used to study the interaction between turbulent discs and protoplanets, eight identical copies of this relaxed disc sector were joined together. The model described in table 2 with azimuthal domain $\pi/2$ (run G5) contained only two copies of the $\pi/4$ sector, and periodic boundary conditions were employed in the azimuthal domain.

Gravitational softening of the protoplanet was employed in all simulations. In runs G1–G4 described in table 2, the softening parameter $b = 0.33H$. For run G5, this was reduced to $b = 0.1H$. For runs G1, G2, and G3, the planet was placed at a radius such that $|r_p - r_*| = 3$ and at azimuthal location $\phi_p = \pi$ in the disc. For runs G4 it was placed such that $(|r_p - r_*|, \phi_p) = (2.5, \pi)$ and for run G5 it was placed at $(|r_p - r_*|, \phi_p) = (2.5, \pi/4)$. All simulations were performed in a rotating frame whose angular velocity equalled that of the circular Keplerian planetary orbit. The unit of time adopted when discussing the results is Ω^{-1} evaluated at $r = 1$, the inner boundary of the computational domain. We note that the orbital period at this radius is $P(r = 1) = 2\pi$, the orbital period of a planet at $r_p = 2.5$ is $P(r = 2.5) \simeq 24$, and the orbital period of a planet at $r_p = 3$ is $P(r = 3) \simeq 32$.

In order to explore the disc–planet interaction over a wider range of parameter space and with higher resolution in the vicinity of the planet, we have adopted a local shearing box approximation. This we describe below.

2.2 Local Shearing Box Simulations

In the shearing box limit (Goldreich & Lynden-Bell 1965) we consider a small Cartesian box centred on the point at which the Keplerian angular velocity is Ω_p . We define local

Cartesian coordinates (x, y, z) with associated unit vectors $(\mathbf{i}, \mathbf{j}, \mathbf{k})$. The direction \mathbf{i} is taken to be outward along the line joining the origin to the central object while \mathbf{k} points in the vertical direction. The direction \mathbf{j} is along the unperturbed rotational shear flow.

The equation of motion may then be written as

$$\frac{\partial \mathbf{v}}{\partial t} + \mathbf{v} \cdot \nabla \mathbf{v} + 2\Omega_p \hat{\mathbf{k}} \times \mathbf{v} - 3\Omega_p^2 x \mathbf{i} = -\frac{\nabla p}{\rho} - \nabla \Phi_p + \frac{(\nabla \times \mathbf{B}) \times \mathbf{B}}{4\pi\rho}. \quad (6)$$

The induction and continuity equations retain the same form as equations (3) and (1) but are of course expressed in component form in the local box centred Cartesian coordinates. We recall that the term $\propto x$ in equation (6) is derived from a first order Taylor expansion about $x = 0$ of the combination of the gravitational acceleration due to the central mass and the centrifugal acceleration (Goldreich & Lynden-Bell 1965). However, as for the global disc simulations, we have neglected the z dependence of the gravitational potential and therefore vertical stratification. Thus in this respect the simulations are of unstratified boxes of the type considered by Hawley, Gammie & Balbus (1995).

Here, when introduced, the planet is located in the centre of the box, thus

$$\Phi_p = -\frac{GM_p}{\sqrt{x^2 + y^2 + b^2}}. \quad (7)$$

In the steady state box with no planet or magnetic field, the equilibrium velocity is due to Keplerian shear and thus

$$\mathbf{v} = (0, -3\Omega_p x/2, 0). \quad (8)$$

We adopt an isothermal equation of state $P = \rho c^2$, with c being the sound speed which is taken to be constant throughout the box.

2.2.1 Initial and Boundary Conditions

The shearing box is presumed to represent a local patch of a differentially rotating disc. Thus the appropriate boundary conditions on the bounding faces $y = \text{constant} = \pm Y$ and $z = \text{constant} = \pm Z$ derive from the requirement of periodicity in the local Cartesian coordinate directions normal to the boundaries. On the boundary faces $x = \text{constant} = \pm X$, the boundary requirement is for periodicity in local shearing coordinates. Thus for any state variable $F(x, y, z)$, the condition is that $F(X, y, z) = F(-X, y - 3\Omega_p X t, z)$. This means that information on one radial boundary face is communicated to the other boundary face at a location in the azimuthal coordinate y shifted by the distance the faces have sheared apart since the start of the simulation, t , (see Hawley, Gammie & Balbus 1995).

For all models adopting a shearing box, the softening parameter was taken as $b = 0.3H$. The potential was flattened (made to attain a constant value in a continuous manner) at large distances from the protoplanet in order to satisfy the periodic boundary conditions. In simulations Ba0–Ba4 (described in table 1) this was done outside the cylinder of radius $3H$ centred on the planet. In simulations Bb1–Bb4 this was done only close to the boundary.

The simulations Ba0–Ba4 occupied a total width $8H$ in x and $4\pi H$ in y . These boxes were found to be large enough to accommodate the scale of the disc response to forcing by the

protoplanet and enable gap formation. But note that interference from protoplanets in neighbouring boxes implied by the periodic boundary conditions is not eliminated entirely. In the small protoplanet mass regime waves propagate between boxes and in the nonlinear regime torques exerted by protoplanets in neighbouring boxes may influence the gap formation process. However, comparison between local and global runs indicates that such effects are not major and do not prevent the box runs from capturing the essential physics.

To examine the effect of varying box size we ran simulations Bb1–Bb4 which were of the same resolution but had twice the extent in y .

All of these models were initiated by imposing a vertical field, with zero net flux through the box, varying sinusoidally in x with a wavelength of H . The amplitude was such that the initial value of the ratio of the total magnetic energy to volume integrated pressure was 0.0025. The initial velocity in the x direction at each grid point was chosen to be the product of a random number between -1.0 and 1.0 and $0.1c$. The initial velocity in the y -direction is given by equation 8, and the z component of velocity was initialized to zero. The unit of time for all simulations was taken to be Ω_p^{-1} . In these units the orbital period at the centre of the box is 2π .

2.3 Dimensionless Variables and Scaling with Planet Mass

It is helpful to write the governing equations for the shearing box in dimensionless form. In this way the dependence of the outcomes of the simulations on planet mass and disc parameters is made clearer (see also Korycansky & Papaloizou 1996). To do this we adopt dimensionless coordinates $(x', y', z') = (x/H, y/H, z/H)$, where the length scale $H = c/\Omega_p$ would correspond to the disc scale height were it vertically stratified and the dimensionless time $t' = \Omega_p t$. We also note that the Keplerian relation $\Omega_p^2 = GM_*/R^3$, may be used to relate the rotation rate of the centre of the box to a putative central mass M_* and orbital radius R . We now introduce the dimensionless velocity, sound speed and planet mass through $\mathbf{v}' = \mathbf{v}/(\Omega_p H)$, $c' = c/(\Omega_p H)$, and $M'_p = M_p R^3/(M_* H^3)$ respectively. As we do not include the self-gravity of the disc in calculating its response, the magnitude of the disc density may be arbitrarily scaled. The models simulated here all start with a uniform density ρ_0 which, together with H , may be used to specify the mass scaling. Then we define a dimensionless density and magnetic field through $\rho' = \rho_0 \rho$ and $\mathbf{B}' = \mathbf{B}/(\Omega_p H \sqrt{4\pi \rho_0})$. The equation of motion may be written in the above dimensionless variables in the form

$$\frac{\partial \mathbf{v}'}{\partial t'} + \mathbf{v}' \cdot \nabla \mathbf{v}' + 2\hat{\mathbf{k}} \times \mathbf{v}' - 3x' \mathbf{i} = -\frac{\nabla(\rho' c'^2)}{\rho'} - \nabla \Phi'_p + \frac{(\nabla \times \mathbf{B}') \times \mathbf{B}'}{\rho'}, \quad (9)$$

where

$$\Phi'_p = -\frac{M'_p}{\sqrt{x'^2 + y'^2 + b'^2}}, \quad (10)$$

with dimensionless softening parameter $b' = b/H$ and of

course the spatial derivatives are with respect to the dimensionless coordinates. Similarly the dimensionless induction equation becomes

$$\frac{\partial \mathbf{B}'}{\partial t'} = \nabla \times (\mathbf{v}' \times \mathbf{B}'). \quad (11)$$

and the dimensionless continuity equation is

$$\frac{\partial \rho'}{\partial t'} + \nabla \cdot (\rho' \mathbf{v}') = 0. \quad (12)$$

We remark that in dimensionless coordinates the boundaries of the box are $x' = \pm X/H$, $y' = \pm Y/H$, $z' = \pm Z/H$. Also if the magnetic field has zero net flux and is dynamo generated and thus a spontaneous product of the simulation, given that the only parameter occurring in equations (9 - 12) is the dimensionless mass $M'_p = M_p R^3/(M_* H^3)$, we should be able to consider the dependence of the time averaged outcome of a simulation to be only on $X/H, Y/H, Z/H$, and $M'_p = M_p R^3/(M_* H^3)$.

For a planet embedded in a box with natural vertical scale H with sufficiently large X/H to incorporate the tidal interaction without interference from other boxes centred on different radii, the only parameters determining long term averaged properties of a simulation should be Y/H and M'_p . Thus for such a quantity Q , we should have $Q = f(Y/H, M_p R^3/(M_* H^3))$.

Note that the above discussion implies that for a box of fixed dimension, the only distinguishing parameter is $M'_p = M_p R^3/(M_* H^3)$. This parameter may also be interpreted as the cube of the ratio of the Hill radius to disc scale height and the condition that $M'_p \gtrsim 1$ leads to the thermal condition of Lin & Papaloizou (1993) that the Hill radius should exceed the disc scale height for gap formation to occur. From Korycansky & Papaloizou (1996) this condition is also required in order that the perturbation due to the protoplanet be non linear.

The above discussion indicates that were we to vary the box size in the azimuthal (y) direction, the condition for gap formation should be of the form $M'_p > f_g(Y/H)$. As gap formation by the same planet in a longer box is expected to be more difficult, we expect f_g to be a non decreasing function of its argument. In order to correspond to a full circle of radius R , we require that $Y = \pi R$.

It is perhaps suggestive to point out that if $f_g(\pi R/H) = 40\alpha(R/H)$, the condition for gap formation indicated above becomes $M_p/M_* > 40\alpha H^2/(R^2)$ which is of the same form as the viscous criterion of Lin & Papaloizou (1993) which was obtained by requiring angular momentum transport due to excited waves to exceed that due to viscosity. However, it is important to note that if we introduce such an α parameter here, it cannot correspond to an imposed viscosity as in Lin & Papaloizou (1993). Instead it must be related to the turbulent transport arising from MHD turbulence. We take it to correspond to a time average of the volume averaged stress $\langle B_x B_y / (4\pi) \rangle$ expressed in units of the volume averaged pressure $\langle P \rangle$, thus corresponding to the Shakura & Sunyaev (1973) parameterization. This procedure is reasonably well defined in the parts of the disc not strongly perturbed by a protoplanet (eg. Paper II). For simulations with zero net magnetic flux $\alpha \sim 5 \times 10^{-3}$ but it takes on larger values when a net poloidal or toroidal flux is imposed (eg. Hawley, Gammie & Balbus 1996; Steinacker & Papaloizou 2002).

Model	z domain	x domain	y domain	t_1	t_2	$(M_p R^3 / (M_* H^3))$	n_z	n_x	n_y
Ba0	$(-H/2, H/2)$	$(-4H, 4H)$	$(-\pi H, 2\pi H)$	0.0	637	0.0	35	261	200
Ba1	$(-H/2, H/2)$	$(-4H, 4H)$	$(-\pi H, 2\pi H)$	354	621	0.1	35	261	200
Ba2	$(-H/2, H/2)$	$(-4H, 4H)$	$(-\pi H, 2\pi H)$	354	644	0.3	35	261	200
Ba3	$(-H/2, H/2)$	$(-4H, 4H)$	$(-\pi H, 2\pi H)$	354	619	1.0	35	261	200
Ba4	$(-H/2, H/2)$	$(-4H, 4H)$	$(-\pi H, 2\pi H)$	354	650	2.0	35	261	200
Bb1	$(-H/2, H/2)$	$(-4H, 4H)$	$(-\pi H, 4\pi H)$	216	392	0.2	35	261	396
Bb2	$(-H/2, H/2)$	$(-4H, 4H)$	$(-\pi H, 4\pi H)$	216	431	0.5	35	261	396
Bb3	$(-H/2, H/2)$	$(-4H, 4H)$	$(-\pi H, 4\pi H)$	216	411	1.0	35	261	396
Bb4	$(-H/2, H/2)$	$(-4H, 4H)$	$(-\pi H, 4\pi H)$	216	485	2.0	35	261	396

Table 1. Parameters of the shearing box simulations: The first column gives the simulation label, the second, third and fourth give the extent of the coordinate domains considered. The first nine simulations were performed in shearing boxes with the x , y , and z domains referring to the Cartesian domains. The last two simulations were global so that in these cases the x , y , and z domains refer to the r , ϕ , and z domains for the cylindrical coordinate system used. The fifth and sixth column give the start and end times if the simulation measured in dimensionless units. Simulations with protoplanets were started by inserting the protoplanet into the turbulent model generated from the simulation Ba0 at time indicated. The seventh column gives the value of $(GM_p / (\Omega^2 H^3))$. The eighth, ninth and tenth columns give the number of computational grid points in the x , y , and z coordinates respectively. These numbers include any ghost zones used to handle boundary conditions.

Adopting $\alpha = 5 \times 10^{-3}$, suggests $f_g(Y/H) \sim 0.07(Y/H)$. We recall that should $0.07(Y/H)$ be less than unity, the requirement of nonlinear perturbation by the protoplanet in order for gap formation to occur is $M_p/M_* > C_t(H/R)^3$, where C_t is a constant of order unity (Korycansky & Papaloizou 1996). Both these conditions can be combined to give the requirement that

$$M_p R^3 / (M_* H^3) > \max(C_t, 0.07(Y/H)) \quad (13)$$

In this way we may see how both the thermal and viscous conditions of Lin & Papaloizou (1993) may be related to the simulations.

3 WAKES AND CHARACTERISTICS

A well known phenomenon found in simulations of protoplanets interacting with laminar discs is a prominent wake that is observed to trail away from the protoplanet eventually becoming a spiral wave propagating away from it (e.g. Kley 1999; Nelson et al 2000; Lubow, Seibert & Artymanyowicz 1999). Such structures, though distorted, are also seen in our simulations of discs with MHD turbulence in which there are strong and highly time variable fluctuations, even for weakly perturbing protoplanets. In view of their importance and persistence we here give a brief discussion of their interpretation as being defined by a characteristic ray emanating from the protoplanet that separates the flow shearing past it into parts causally connected and not causally connected by waves. The wakes thus naturally correspond to the location a strong wave sent out from the protoplanet into the flow shearing past it.

3.1 The Characteristic Rays

The set of basic equations defined by (1), (2) and (3) are well known to form a hyperbolic set which can be written in the standard form (Courant & Hilbert 1962)

$$\sum_{i,j} \left(A_{ij}^{(k)} \frac{\partial U_i}{\partial x_j} \right) + B^{(k)} = 0 \quad (k = 1, 2, \dots, n). \quad (14)$$

Here the set of equations (1), (2) and (3) are arranged into a set of n simultaneous first order PDEs for the n components U_i of \mathbf{U} which are in turn composed of ρ together with the components of \mathbf{B} and \mathbf{v} . The x_j ($j = 1 - 4$) are the three spatial coordinates and the time t respectively. The characteristic rays, applicable to both the global and local formulation may be found by first obtaining the local dispersion relation associated with (14). To do this one sets $U_i = U_{i0} \exp(ik_j x_j - i\omega t)$ under the assumption that the magnitudes of the components of the wave vector k_l ($l = 1, 2, 3$) $\equiv \mathbf{k} = (k_x, k_y, k_z)$ and the wave frequency $|\omega|$ are very large. The dispersion relation is then given by the vanishing of a determinant of coefficients $|A_{ij}^{(k)} k_j - A_{i4}^{(k)} \omega| = 0$. As is very well known (eg. Campbell 1997) this dispersion relation leads to three distinct wave modes. The first are the Alfvén waves propagating in opposite directions which have $\omega = -\mathbf{k} \cdot \mathbf{v} \pm \mathbf{k} \cdot \mathbf{v}_A$, with $\mathbf{v}_A = v_A \mathbf{B} / |\mathbf{B}|$, where v_A is the Alfvén speed being such that $v_A^2 = |\mathbf{B}|^2 / (4\pi\rho)$. The other modes are fast and slow magnetosonic waves which satisfy

$$(\omega + \mathbf{k} \cdot \mathbf{v})^2 = \frac{k^2(c^2 + v_A^2)}{2} \pm \frac{\sqrt{k^4(c^4 + v_A^4) - 2k^2c^2(\mathbf{k} \cdot \mathbf{v}_A)^2}}{2}. \quad (15)$$

Here $k = |\mathbf{k}|$ and we note that the frequency, ω occurs added to the quantity $\mathbf{k} \cdot \mathbf{v}$ in these relations. This is due to the Doppler shift occurring on account of the motion of the fluid.

For each of these waves we may specify $\omega = \omega(\mathbf{k}, \mathbf{r}, t)$. Then the characteristic rays follow from integrating the equations of geometric optics (e.g. Whitham 1999)

$$\frac{d\mathbf{r}}{dt} = \frac{\partial \omega}{\partial \mathbf{k}}, \quad \text{and} \quad \frac{d\mathbf{k}}{dt} = -\frac{\partial \omega}{\partial \mathbf{r}}. \quad (16)$$

To be specific, we here concentrate on the fast magnetosonic mode which in our case leads to the most rapid communication. Further, as for the most part the magnetic energy is on the order of one percent of the thermal energy,

Model	ϕ domain	H/r	M_p/M_*	$(M_p R^3 / (M_* H^3))$	n_r	n_ϕ	n_z
G1	2π	0.07	1×10^{-5}	0.03	450	1092	40
G2	2π	0.07	3×10^{-5}	0.09	450	1092	40
G3	2π	0.07	1×10^{-4}	0.30	450	1092	40
G4	2π	0.07	3×10^{-3}	8.75	450	1092	40
G5	$\pi/2$	0.07	3×10^{-3}	8.75	450	276	40

Table 2. Parameters of the global simulations: The first column gives the simulation label, the second gives the extent of the azimuthal domain, the third gives the H/r value of the disc, and the fourth gives the protoplanet-star mass ratio. The fifth gives the ratio of M_p/M_* to $(H/r)^3$. The sixth, seventh, and eighth columns describe the number of grid cells used in each coordinate direction.

we shall neglect the field so that the mode becomes an ordinary sound wave such that

$$\omega = -\mathbf{k} \cdot \mathbf{v} + ck. \quad (17)$$

We consider the general situation to be one for which the flow streams past the protoplanet from $y > 0$ to $y < 0$ for $x > 0$ and with the flow moving in the opposite sense for $x < 0$. Considering without loss of generality the case $y > 0$, when the flow streams past supersonically, if we neglect dependence on z , it is divided into two parts by the characteristic originating close to the planet from the point with $y = 0$ and the smallest possible positive value of x at which the flow speed is equal to the wave speed. If the planet had no gravity, the fluid that is upstream of this characteristic would be unaware of the presence of the planet.

The fluid that first knows about the planet, namely that on the characteristic is a natural channel for waves to propagate that are excited by the planet which is why this region is so prominent in the simulations. Note that the concept of characteristic rays is robust in that it can apply to a general time dependent fluid with turbulence. Also with z dependence restored we would expect the fluid to be divided by a surface made up from many rays rather than a single ray which is of the same form independent of z . This would lead to some blurring of the wake.

A characteristic ray is defined by its point of origin (here specified above) and the value of \mathbf{k} . However, note that only the ratio of the components and not the magnitude matters. The natural choice is $k_z = 0$, and k_y/k_x such that $\omega = 0$. This is because we expect a zero frequency wave to be excited by the planet in a frame in which that is at rest. However, note that in a turbulent time dependent situation ω would not be constant.

The simplest situation is one when the flow is time independent and the velocity is given by (8). In that case it follows from equations (16) that both $\omega = 0$ and k_y are constant.

It further follows from equations (16) that the characteristic rays then satisfy

$$\frac{dy}{dx} = -\sqrt{v_y^2/c^2 - 1}. \quad (18)$$

Using equation (8) for v_y and integrating we obtain for the characteristic ray for $x > x_0$

$$y/x_0 = -\frac{x}{2x_0} \sqrt{x^2/x_0^2 - 1} + \frac{1}{2} \ln \left(\sqrt{x^2/x_0^2 - 1} + x/x_0 \right), \quad (19)$$

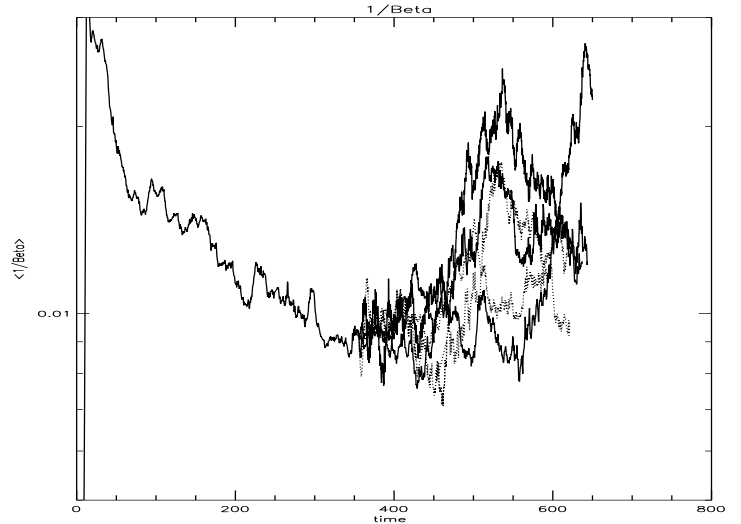


Figure 1. The ratio of the total magnetic energy to the volume integrated pressure, $\langle 1/\beta \rangle$, is plotted as a function of time for models Ba0, Ba1, Ba2, Ba3, and Ba4. The plots begin to separate after the protoplanet is inserted at time 354.. At time 500 the curves correspond to simulations Ba4, Ba1, Ba2, Ba3 and Ba0 with decreasing values of $\langle 1/\beta \rangle$ respectively. Although there are large fluctuations, the maximum variation at any time is factor of 3. This is significantly smaller than the density depression in the deepest gap (see figure 10).

with $x_0 = 2H/3$. To complete the picture we remark that the characteristic for $x < 0$, can be found from the condition $y(-x) = -y(x)$.

We comment that the computational domains in all of our simulations are extensive enough to contain the characteristic associated with the waves emitted by an exciting object, be it turbulent fluctuations or a protoplanet (i.e. x exceeds $2/s3H$ by a significant margin).

4 NUMERICAL PROCEDURE

The numerical scheme that we employ is based on a spatially second-order accurate method that computes the advection using the monotonic transport algorithm (Van Leer 1977). The MHD section of the code uses the method of characteristics constrained transport (MOCCT) as outlined in Hawley & Stone (1995) and implemented in the ZEUS

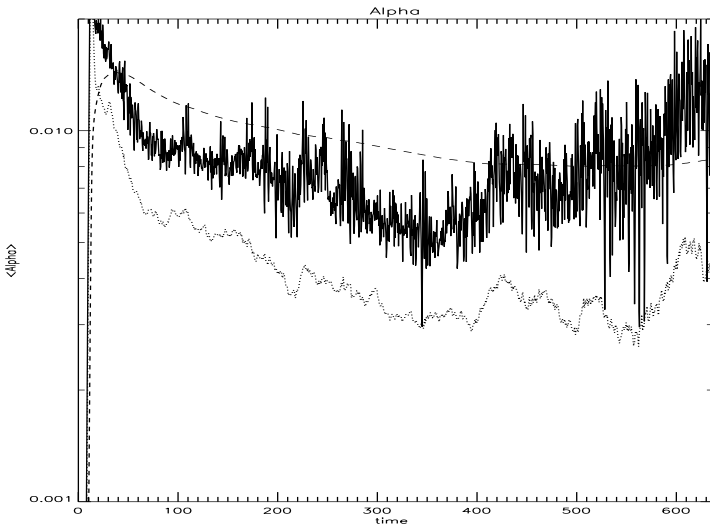


Figure 2. The volume averaged stress parameter $\langle \alpha \rangle$ is plotted as a function of time for model Ba0 which has no protoplanet. The noisy full curve contains contributions from both the magnetic and Reynolds' stresses while the dotted curve gives the magnetic contribution. The dashed curve gives the running time average of the total stress. The large initial values are due to the initial strong instability which produces a channel phase. However, after about four orbits at the centre of the box, the running time average is within a factor of two of the final value.

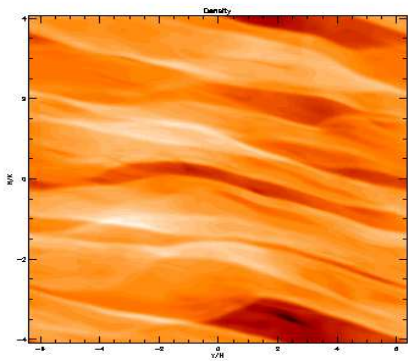


Figure 3. Density contour plot in a (x, y) plane for simulation Ba0 which has no embedded protoplanet. The extensions are $8H$ in the x direction and $4\pi H$ in the y direction. The plot applies near the end of the simulation. The range of variation in the density is about a factor of three. This is typical of what is obtained in any (x, y) plane once a statistically steady state turbulence is set up. Note the trailing elongated structures.

code. The code has been developed from a version of NIR-VANA originally written by U. Ziegler (see SP, Ziegler & Rüdiger (2000), and references therein)

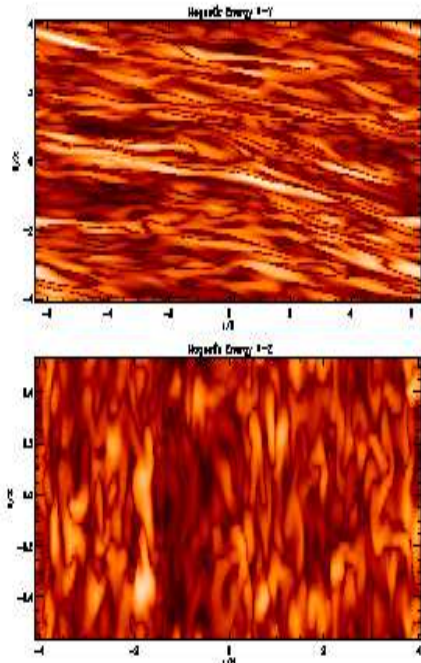


Figure 4. Contours of magnetic energy density corresponding to the plot in figure 3. The upper plot corresponds to the (x, y) plane illustrated in figure 3 while the lower plot is taken in a characteristic (x, z) plane. The extensions are H in the z direction and $8H$ in the x direction. Due to regions of very small magnetic field, the range of variation of magnetic energy density is much larger than that of the density being as much as $\sim 10^7$. These plots are typical of what is found for the turbulence once it has reached a statistically steady state. Note that trailing elongated features are also apparent in the distribution of the magnetic energy density.

4.1 Vertically and Horizontally Averaged Stresses and Angular Momentum Transport

In order to describe average properties of the turbulent models, following papers I and II we use quantities that are vertically and azimuthally averaged over the (y, z) domain for the shearing boxes or the (ϕ, z) domain for the global simulations (e.g. Hawley 2000). Thus we may consider $y \equiv \phi$ and $x \equiv r$ in these cases. Sometimes an additional time average may be adopted. The vertical and azimuthal average of some quantity Q is then defined through

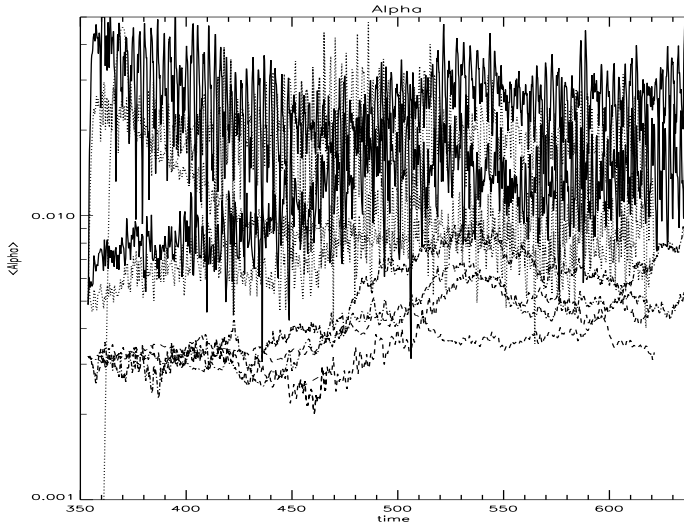


Figure 5. The volume averaged total stress parameter $\langle \alpha \rangle$ is plotted as a function of time for models Ba1, Ba2, Ba3, and Ba4. The plots begin from the moment the protoplanet is inserted. The noisy upper curves contain contributions from both the magnetic and Reynolds' stresses. They can be identified at early times as for Ba4 (uppermost full curve), Ba3 (uppermost dotted curve), Ba2 (next highest full curve), Ba1 (next highest dotted curve). The lower and much less noisy curves give the magnetic contribution. These are similar until they separate at about time 500. At this time they may be identified with increasing values of the stress parameter as associated with Ba1, Ba3, Ba2 and Ba4 respectively. The values of the total $\langle \alpha \rangle$ show a sharp increase when the protoplanet is inserted in the cases with higher mass protoplanets on account of the excitation of density waves which provide angular momentum transport.

$$\overline{Q} = \frac{\int \rho Q dz dy}{\int \rho dz dy}. \quad (20)$$

The disc surface density is given by

$$\Sigma = \frac{1}{2Y} \int \rho dz dy. \quad (21)$$

The vertically and azimuthally averaged Maxwell and Reynolds stresses, are given by:

$$T_M = 2Y\Sigma \overline{\left(\frac{B_x B_y}{4\pi\rho} \right)} \quad (22)$$

and

$$T_{Re} = 2Y\Sigma \overline{\delta v_x \delta v_y}. \quad (23)$$

Here the velocity fluctuations δv_x and δv_y are defined through,

$$\delta v_x = v_x - \overline{v_x}, \quad (24)$$

$$\delta v_y = v_y - \overline{v_y}. \quad (25)$$

The horizontally and vertically averaged Shakura & Sunyaev (1973) α stress parameter appropriate to the total stress is given by

$$\alpha = \frac{T_{Re} - T_M}{2Y\Sigma(P/\rho)}, \quad (26)$$

The angular momentum flow across a line of constant x is given by

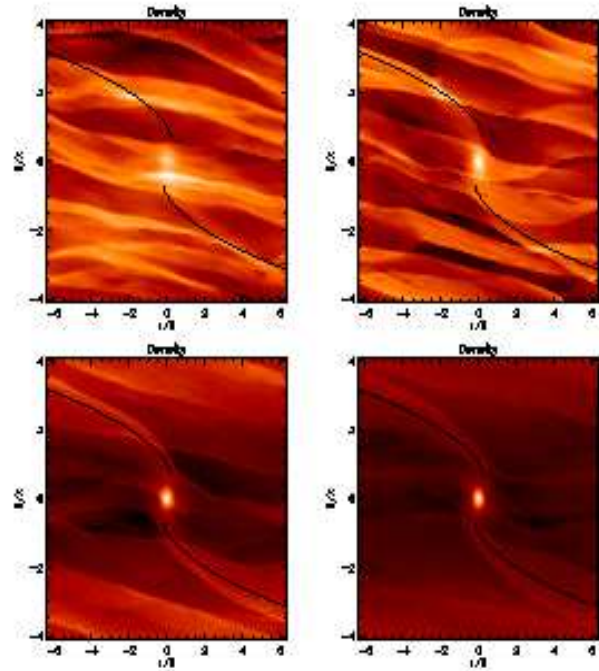


Figure 6. Density contour plots in a typical (x, y) plane for simulations Ba1, top left, Ba2 top right, Ba3 bottom left, and Ba4 bottom right taken near the end of the simulations. These had $M_p R^3 / (M_* H^3) = 0.1, 0.3, 1.0$ and 2.0 respectively. As $M_p R^3 / (M_* H^3)$ increases, the wake becomes more prominent, material is accreted by the protoplanet and is pushed toward the radial boundaries as a gap is formed. The location of the characteristic ray given by equation (19) is also plotted. The qualitative structure seen in these simulations is maintained once a quasi steady state has been attained.

$$\mathcal{F} = \Sigma W \overline{\alpha P / \rho}. \quad (27)$$

Here $W = R^2$ for the shearing box simulations or $W = r^2$ for the global simulations.

5 NUMERICAL RESULTS

We now present numerical results for the evolution of the simulations.

5.1 Shearing Box Simulations

All of the shearing boxes are derived from the simulation Ba0 which was carried out without a protoplanet. It settled

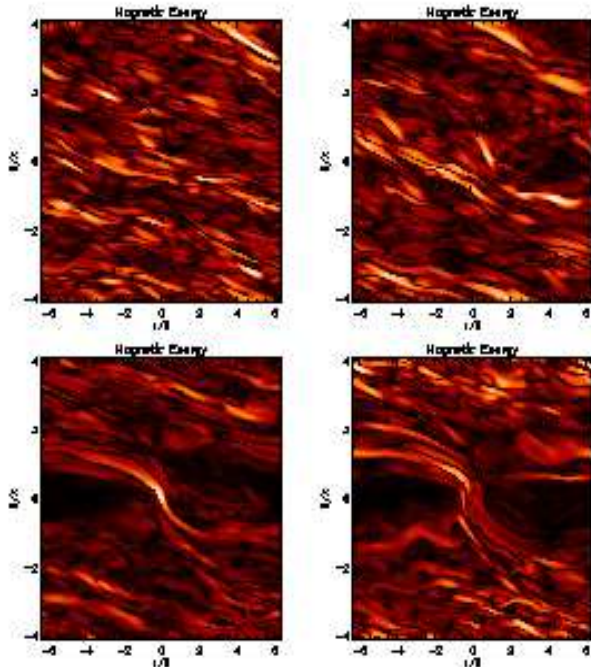


Figure 7. As in figure 6 but in this case magnetic energy density contours are plotted. As $M_p R^3 / (M_* H^3)$ increases and a gap forms, the magnetic energy generally decreases in the gap region. However, some remains concentrated in regions near the high density wakes. The qualitative structure seen in these simulations is maintained once a quasi steady state has been attained.

into a quasi steady state with conserved zero net flux and dynamo maintained turbulence as has been described by others (e.g. Hawley, Gammie & Balbus 1996). This model was run for 100 orbits at the box centre. The ratio of the total magnetic energy to the volume integrated pressure, $\int \mathbf{B}^2 / (8\pi) dV / \int P dV = \langle 1/\beta \rangle$, is plotted as a function of time in figure 1.

After time 354 this model was used to provide initial conditions for models with protoplanets of varying masses. Simulations Ba1, Ba2, Ba3, and Ba4 were begun in this way with $M_p R^3 / (M_* H^3) = 0.1, 0.3, 1.0$ and 2.0 respectively. We also plot $\int \mathbf{B}^2 / (8\pi) dV / \int P dV = \langle 1/\beta \rangle$ as a function of time in figure 1 for models Ba1, Ba2, Ba3, and Ba4. The plots begin to separate from each other shortly after the simulations with protoplanets have begun. Note that although $\langle 1/\beta \rangle$ is in general confined between 0.008 and 0.02 with or without a protoplanet, there are strong fluctuations on a range of timescales down to the orbital timescale. The ex-

istence of such fluctuations and the difficulties they cause for defining mean state variables for the turbulent flow has been emphasised recently by several authors (e.g. papers I and II; Winters, Balbus & Hawley 2003; Armitage 2002).

The volume averaged stress parameter $\langle \alpha \rangle$ is plotted as a function of time for model Ba0 in figure 2. As for $\langle 1/\beta \rangle$, erratic fluctuations are seen. The sum of the magnetic and Reynolds' stresses nearly always exceeds the magnetic contribution for which the short term fluctuations are significantly less severe. In these respects the behaviour of local and global simulations are similar (Steinacker & Papaloizou 2002, papers I and II, and section 5.2). The running time average of $\langle \alpha \rangle$ is also plotted and this shows much smoother behaviour. Somewhat large initial values occur because of the initial strong instability which produced a channel phase. However, after about four orbits at the centre of the box, the running time average is within a factor of two of its final value of 0.008. This value is in agreement with that given in Winters, Balbus & Hawley (2003). But note that the running time average still shows variations at the 10 percent level after 100 orbits.

The pattern of turbulence in simulation Ba0 is established after several orbits. A typical density contour plot in a (x, y) plane is presented in figure 3 near the end of the simulation. The range of variation in the density in this plane is about a factor of three. The situation illustrated here is typical of what is obtained in any (x, y) plane once a statistically steady state turbulence is set up. Elongated trailing structures are noticeable. We plot contours of the magnetic energy density in figure 4 which correspond to the plot in figure 3. The upper plot corresponds to the (x, y) plane illustrated in figure 3 while the lower plot is taken in a characteristic (x, z) plane. Due to the existence of regions where the magnetic field is near zero, the range of the magnetic energy density is much larger than that of the mass density, being as much as $\sim 10^7$. The plots are typical of what is found once the turbulence has reached a quasi steady state.

When a protoplanet is placed in the centre of the box waves are excited that cause outward angular momentum transport. These waves also have an associated Reynolds' stress (e.g. Papaloizou & Lin 1984) and may affect the underlying turbulence.

The volume averaged total stress parameter $\langle \alpha \rangle$ is plotted as a function of time for models Ba1, Ba2, Ba3, and Ba4 in figure 5. The plots commence from the moment when the protoplanet was introduced. The introduction causes the excitation of a wave and an increase in the Reynolds' stress which in turn increases the total stress. This is particularly noticeable in simulations Ba3 and Ba4 which have $M_p R^3 / (M_* H^3) = 1.0$ and 2.0 respectively and so have large enough protoplanets to form a gap. This behaviour was also found in the simulation of a 5 Jupiter mass planet in a disc with $H/R = 0.1$ presented in paper II and in the global simulations described in section 5.2. After a sharp initial rise the volume averaged Reynolds' stress here tends to decrease as a gap is opened and material is moved away from the protoplanet. The much less noisy volume averaged magnetic stresses are also plotted in figure 5. These behave similarly for each of the simulations Ba1, Ba2, Ba3 and Ba4 but they then separate at about time 500. Although simulation Ba4 which has the highest protoplanet mass also tends to have

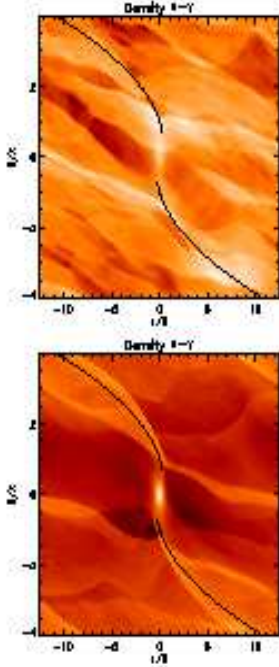


Figure 8. Plots corresponding to those in figure 6 but for models Bb1, Bb2, Bb3, Bb4. A similar sequence is indicated.

the highest volume averaged magnetic stress, there is no other such correlation between magnetic stress and protoplanet mass and so this may not be significant.

Although, as we have indicated above, strong fluctuations are indeed the rule, there are definite behavioural trends as the protoplanet mass increases. To illustrate these, density contour plots in a typical (x, y) plane for simulations Ba1, Ba2, Ba3 and Ba4 near the end of the simulations are shown in figure 6. It can be seen that as $M_p R^3 / (M_* H^3)$ increases, the wake becomes more prominent. It can be seen that this wake approximately coincides with that given by equation (19) derived from the discussion about characteristic rays. The wake is the first observable manifestation of the presence of the protoplanet and can be just traced in simulation Ba1 for which $M_p R^3 / (M_* H^3) = 0.1$. This is well before any effects can be seen in the magnetic energy density contours or a gap forms. In figure 7 we plot the magnetic energy density contours corresponding to the density plots in figure 6.

As $M_p R^3 / (M_* H^3)$ increases and a gap forms, the magnetic energy generally decreases in the gap region. Where

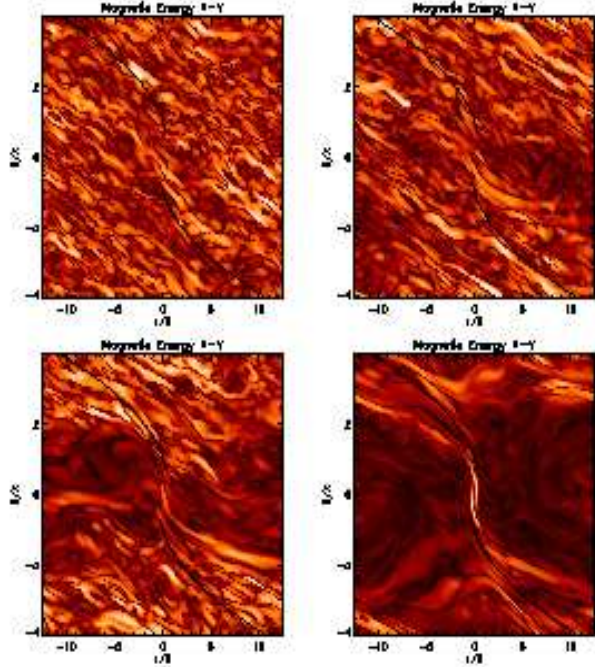


Figure 9. Plots corresponding to those in figure 7 but for models Bb1, Bb2, Bb3, Bb4. A similar sequence is indicated.

it remains it tends to be concentrated in regions near the high density wakes. This tendency was also apparent in the global simulation of paper II and is also observed in the global simulations G4 and G5 described in section 5.2.

To examine the effect of lengthening the box in the azimuthal or y direction, we carried out simulations Bb1, Bb2, Bb3 and Bb4 which had the same resolution as Ba0, Ba1, Ba2, Ba3 and Ba4 but were extended by a factor of 2 to 8π in y . However, because of the obvious increased computational demands, these simulations were run for shorter times. Each was begun by taking simulation Ba0 at a time 216, extending it to 8π in y by using the appropriate periodicity condition and inserting protoplanets with masses given in table 1. Mass density and magnetic energy density plots are plotted in figures 8 and 9 respectively. A similar behavioural trend to that found for the shorter boxes is noted.

To illustrate the gap formation process the density averaged over y and z is plotted against x for simulations Ba0, Ba1, Ba2, Ba3 and Ba4 at a moment near the end of the simulations in figure 10. As $M_p R^3 / (M_* H^3)$ increases, material is pushed toward the radial boundaries by the action of

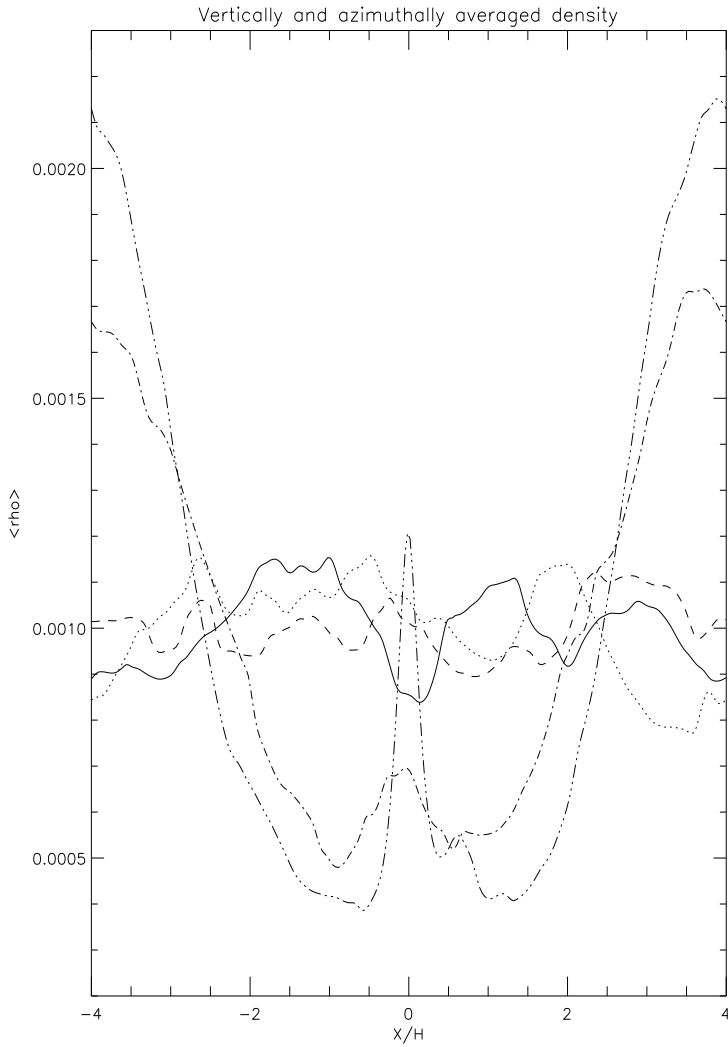


Figure 10. Density averaged over y and z plotted against x for simulations Ba0 full curve, Ba1 dotted curve, Ba2 dashed curve, Ba3 dot dashed curve, and Ba4 triple dot dashed curve, taken near the end of the simulations. These had $M_p R^3 / (M_* H^3) = 0.1, 0.3, 1.0$ and 2.0 respectively. The plots show that $M_p R^3 / (M_* H^3)$ increases, material is accreted by the protoplanet and is pushed toward the radial boundaries as a gap is formed. Such a gap is noticeable in simulations Ba3 and Ba4 but not in simulations Ba1 and Ba2 which have a very similar behaviour of the mean density to that found in simulation Ba0 which had no protoplanet. Although there are turbulent fluctuations the same structure persists once a quasi steady state is achieved.

the wave stresses and a gap is formed. In addition it is apparent that there is some accretion onto the protoplanet in the sense that some material settles onto it becoming bound. The horizontally and vertically averaged density profiles associated with Ba0, Ba1 and Ba2 indicate no sign of a gap with the variations between them similar to what would be seen for any one of them at different times. However a persistent gap is clearly visible for runs Ba3 and Ba4 for which $M_p R^3 / (M_* H^3) > 1$.

The horizontally and vertically averaged stress parameter corresponding to the plots in figure 10 is plotted against

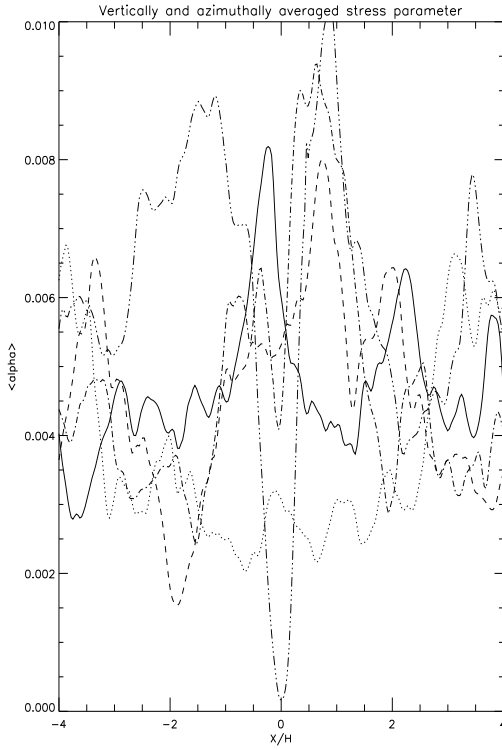


Figure 11. The stress parameter averaged over y and z plotted against x for simulations Ba0 full curve, Ba1 dotted curve, Ba2 dashed curve, Ba3 dot dashed curve, and Ba4 triple dot dashed curve, taken near the end of the simulations. Although there are erratic fluctuations, the variation in $\langle \alpha \rangle$ among the different simulations is typically less than that found in the density in the gap region. This is consistent with a general reduction of magnetic energy density and stress in that region when a gap is formed.

x for simulations Ba0, Ba1, Ba2, Ba3 and Ba4 in figure 11. Although there are erratic fluctuations, the range of variation in $\langle \alpha \rangle$ between the simulations is typically less than that found in the density when there is a gap. This is consistent with a tendency for there to be a general reduction of magnetic energy and stress in a gap region that roughly scales with the decrease in gas density and pressure there.

We have also compared the structure of the gap near the end of the simulation Ba4 with that obtained from a laminar simulation with no magnetic field but uniform anomalous Navier Stokes viscosity corresponding to the time average value of $\alpha = 0.008$ obtained from run Ba0 which had no planet. We emphasize that such a time average has no clear physical connection with the behaviour of simulation Ba4 nonetheless we perform the comparison for general interest.

In figure 12 we plot the azimuthally and vertically averaged density profile at the end of simulation Ba4 together with plots obtained from laminar disc runs with $\alpha = 0.008$ and no viscosity which were run for the same times with the perturbing planet which had $M_p R^3 / (M_* H^3) = 2$. These have been scaled to have the same magnitude at the box edges.

As expected, the inviscid non magnetic run produces a deeper and wider gap than the others. The run with the imposed $\alpha = 0.008$ produces a somewhat narrower gap than the MHD run Ba4 which in this way behaves as if it had

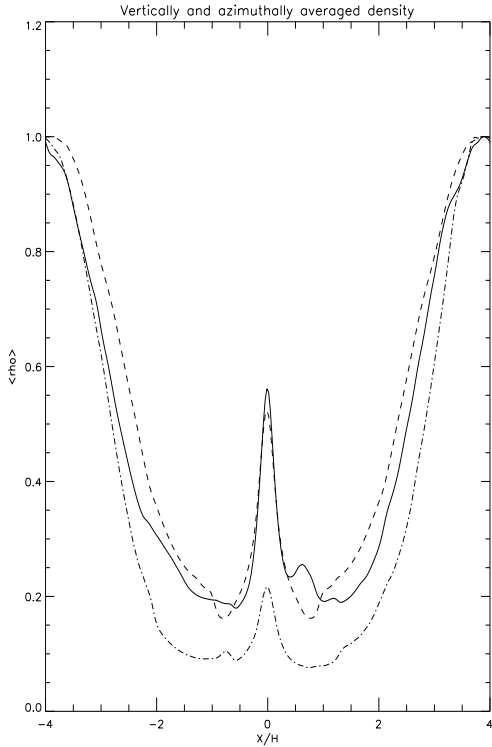


Figure 12. The density averaged over y and z plotted against x for simulation Ba4 full curve, the laminar disc simulation with $\alpha = 0.008$, dashed curve and the inviscid laminar simulation, dot dashed curve, taken near the end of the simulations. The inviscid case has the deepest gap and the case with $\alpha = 0.008$ the narrowest.

lower viscosity. This effect was also found for the global simulation with 5 Jupiter masses in paper II. However, in our case there is slightly more material accreted onto the planet than the laminar viscous case.

Finally we examine the flow in the coorbital region to check for the appearance of circulating horse shoe like trajectories in that region. Velocity vectors in typical (x, y) planes for simulations Ba1, weakly perturbed with $M_p R^3 / (M_* H^3) = 0.1$ and Ba3, strongly perturbed with $M_p R^3 / (M_* H^3) = 2$ are presented in figures 13 and 14 respectively. Circulating trajectories are apparent in the case of Ba3 indicating the existence of a coorbital dynamics. However, the flow pattern appears complex with circulating eddies and multiple shocks. Furthermore we find no indication of a circulating flow around the protoplanet within the Hill sphere. This may be because of a magnetic braking effect already discussed in paper II (also see discussion in section 5.2).

5.2 Global Simulations

In this section we describe the results obtained from the global simulations. We begin by discussing the underlying turbulent disc model, before describing the interaction between protoplanets and global turbulent discs.

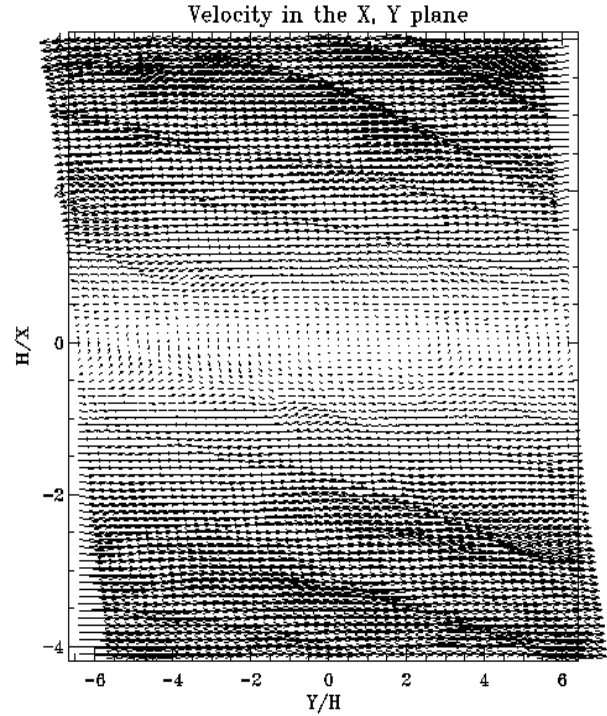


Figure 13. Velocity vectors in a typical (x, y) plane near the end of simulation Ba1 with $M_p R^3 / (M_* H^3) = 0.1$. The perturbation due to the protoplanet is too weak for the existence of horse shoe trajectories that do not cross the whole y domain to be manifest.

5.2.1 Global Turbulent Disc Model

The physical parameters of the global disc model are described in section 2.1. The initial disc model had a $\pi/4$ azimuthal domain, with an imposed zero-net flux toroidal field that varied sinusoidally with radius. The initial value of the ratio of the total magnetic energy to the volume integrated pressure, $\int \mathbf{B}^2 / (8\pi) dV / \int P dV = \langle 1/\beta \rangle = 0.032$. The time evolution of this quantity is shown in figure 15. It is clear that the initially high magnetic energy decreases as the initially imposed magnetic field undergoes reconnection, and $\langle 1/\beta \rangle$ reaches a saturated value of $\langle 1/\beta \rangle \simeq 0.011$ once the turbulence reaches a statistical steady state.

Figure 16 shows the time evolution of the volume averaged Shakura-Sunyaev stress parameter α defined by equation 26. The solid line represents the Maxwell stress, the dotted line represents the Reynolds stress, and the dashed

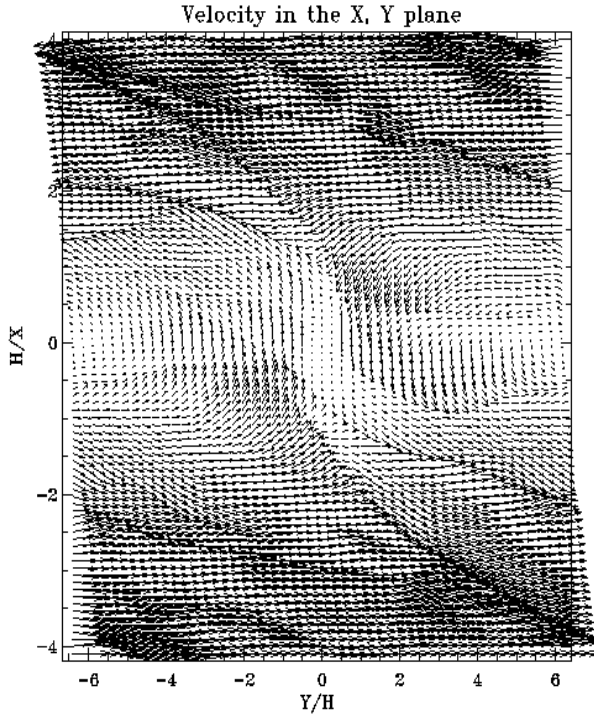


Figure 14. Velocity vectors in a typical (x, y) plane for simulation Ba3 with $M_p R^3 / (M_* H^3) = 2$. The perturbation due to the protoplanet is sufficient for the existence of horse shoe trajectories restricted to a subset of the y domain to be manifest.

line represents the sum of these. It is clear that as the disc becomes unstable to the MRI, the stresses increase initially, but then decrease to a saturated state corresponding to $\alpha \simeq 7 \times 10^{-3}$.

The radial distribution of α , time averaged for a short period of time (one orbit at $r = 1$) is shown in figure 17. As expected this is a rapidly varying quantity as a function of both space and time due to the turbulence (see also paper I).

The final state of the disc model shown in figures 15 – 17 was used as the initial condition for simulations that examine the interaction between turbulent discs and embedded protoplanets. Models G1 – G4 used full 2π azimuthal domains that were constructed by patching eight copies of the $\pi/4$ turbulent disc model together. Model G5, which had a restricted azimuthal domain of $\pi/2$, consisted of two copies of the relaxed, turbulent disc model patched together, with

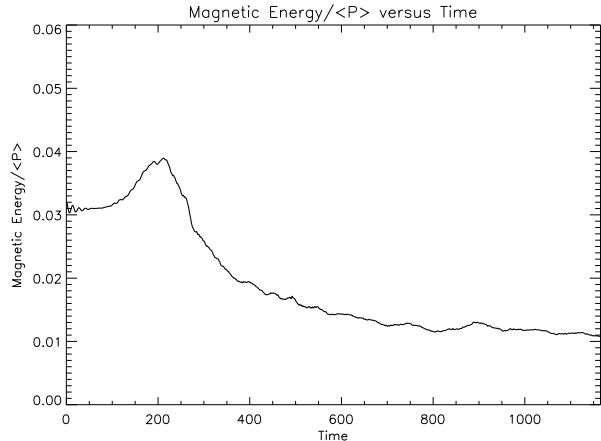


Figure 15. This figure shows the evolution of $\langle 1/\beta \rangle$ for the global disc model.

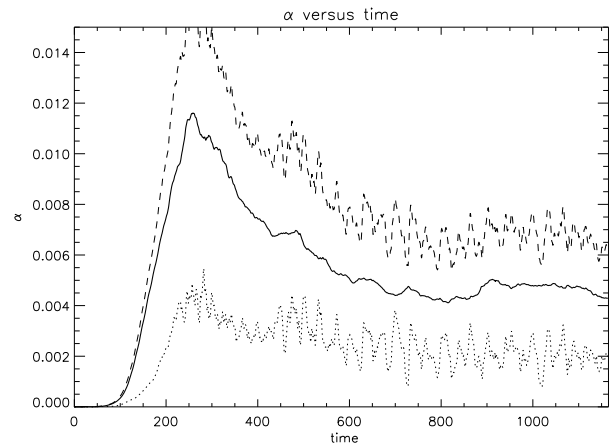


Figure 16. This figure shows the evolution of $\langle \alpha \rangle$ for the global disc model. The solid line represents the Maxwell stress, the dotted line represents the Reynolds stress, and the dashed line represents the total stress.

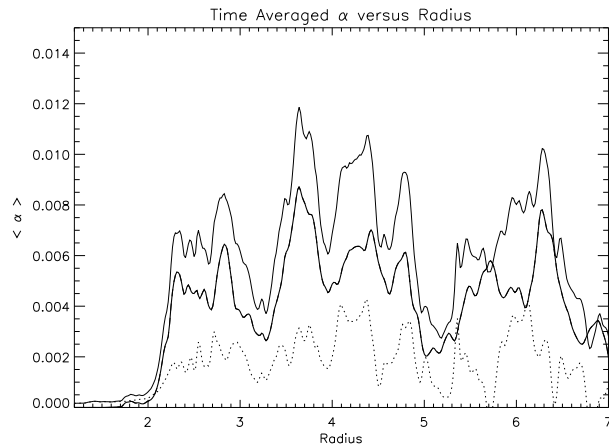


Figure 17. This figure shows the radial profile of $\langle \alpha \rangle$ for the global disc model. The heavy solid line represents the Maxwell stress, the dotted line represents the Reynolds stress, and the thin solid line represents the total stress.

periodic boundary conditions in the azimuthal direction being employed. These simulations are described below.

5.2.2 Global Models with Embedded Protoplanets

In this section we present the results from simulations labeled as G1 – G5 in table 2. The aim is to examine how the disc properties change as a function of planet mass (or alternatively as a function of $(M_p/M_*)/(H/r)^3$), moving from a situation where the protoplanet induces linear perturbations in the disc (e.g. run G1) through to a scenario in which the planet perturbation is nonlinear (e.g. run G5). In particular, we are interested in how the appearance of the spiral density waves vary, how the morphology of the magnetic field changes in the vicinity of the planet, when gap formation arises in a global disc model, and the impact of the protoplanet on the velocity field in the disc. We are also interested in how the results of similar local and global simulations compare.

When discussing the results of the global simulations we will concentrate on the runs G1, G2, G3, and G5. Run G4 adopted the exact same physical parameters as run G5, except that the azimuthal domain in G5 ran from 0 to $\pi/2$, rather than being a full 2π domain. This means that we were able to run simulation G5 for $\simeq 60$ planetary orbits because of the lower computational cost, whereas run G4 was only run for $\simeq 11$ planetary orbits. We therefore give the results of run G5 higher prominence in our discussion, whilst noting that the results obtained in run G4 are in good qualitative agreement with G5.

Figure 18 shows contour plots of the midplane density distribution in the vicinity of the protoplanet for the runs G1, G2, G3, and G5, respectively. In the first panel it is clear that the presence of the planet in the disc is essentially undetectable since the density perturbations induced by the turbulence are of higher amplitude than the spiral waves excited by the protoplanet. The value of $(M_p/M_*)/(H/r)^3$ in this case is 0.03, with the protoplanet mass corresponding to ~ 3 Earth masses (assuming a Solar mass central star). The second panel, corresponding to run G2, shows that the presence of the protoplanet is just about detectable, but the amplitude of perturbations due to the turbulence still exceed the spiral waves induced by the protoplanet. The protoplanet mass in this case is equivalent to ~ 10 Earth masses. The third panel corresponds to run G3, for which the protoplanet mass is equivalent to ~ 30 Earth masses. The presence of the protoplanet in this case is clearly detectable, with the spiral waves being of similar amplitude to the turbulent wakes. The fourth panel shows the results from run G5, in which the protoplanet mass corresponds to 3 Jupiter masses. In this case the disc–protoplanet interaction leads to gap formation since the interaction is strongly nonlinear ($(M_p/M_*)/(H/r)^3 \simeq 8$ in this case). Overall the results here are in very good agreement with those obtained in the shearing box runs, in that they show the same consistent pattern of behaviour with increasing values of $(M_p/M_*)/(H/r)^3$.

We next consider the effect of the protoplanet on the magnetic field. Figure 19 shows contour plots of $|\mathbf{B}|^2$ for the runs G1, G2, G3, and G5. Strong variation in magnetic field strength arises due to the turbulence, as found in the shearing box runs, and the plots show that the magnetic field is largely unaffected by the presence of the embedded proto-

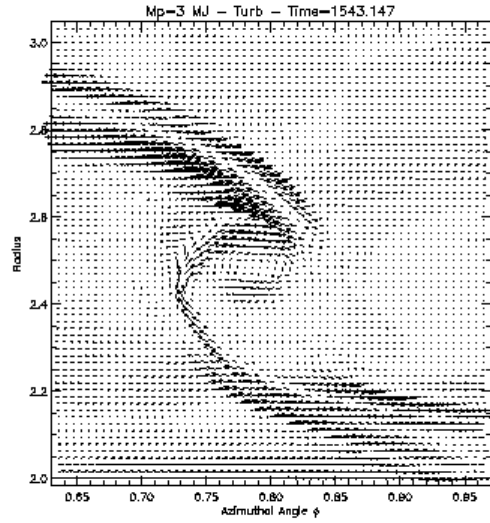


Figure 20. This figure shows magnetic field vectors in the vicinity of the protoplanet for run G5. The compression and ordering of the field due to the spiral shocks is apparent, as is the advection of magnetic flux into the planet Hill sphere.

planets in runs G1, G2, G3. However, the last panel, corresponding to run G5, clearly shows that the magnetic field strength is increased near the spiral shock waves induced by the more massive planet, in agreement with results obtained in paper II and those obtained by the shearing box runs. In general, the magnetic energy and stress decrease in the gap region as the density and pressure decrease, but the disordered, turbulent magnetic field close to the planet becomes ordered and compressed in the spiral wakes, leading to a significant increase in the magnetic stress there. This effect is shown more clearly in figure 20 which shows a snapshot of the magnetic field vectors in run G5. This illustrates how the field becomes compressed and ordered as the gas travels through the spiral shocks, and also shows how the magnetic field is advected into the protoplanet Hill sphere with gas that accretes onto the protoplanet. The effect that the field modification has on the vertically and azimuthally averaged magnetic stress is illustrated by figure 21 which shows the time averaged contribution to α from the magnetic stress as a function of radius. It is clear that the compression of the field along with reduction of the density and pressure in the gap leads to an enhanced α value there.

We now consider how the presence of the protoplanet affects the radial density distribution in the disc. Figure 22 shows the azimuthally averaged midplane density distribution for the runs G1, G2, G3, and G5, as well as the initial $1/r$ density profile. This plot shows that some accretion though the disc has occurred during its initial relaxation

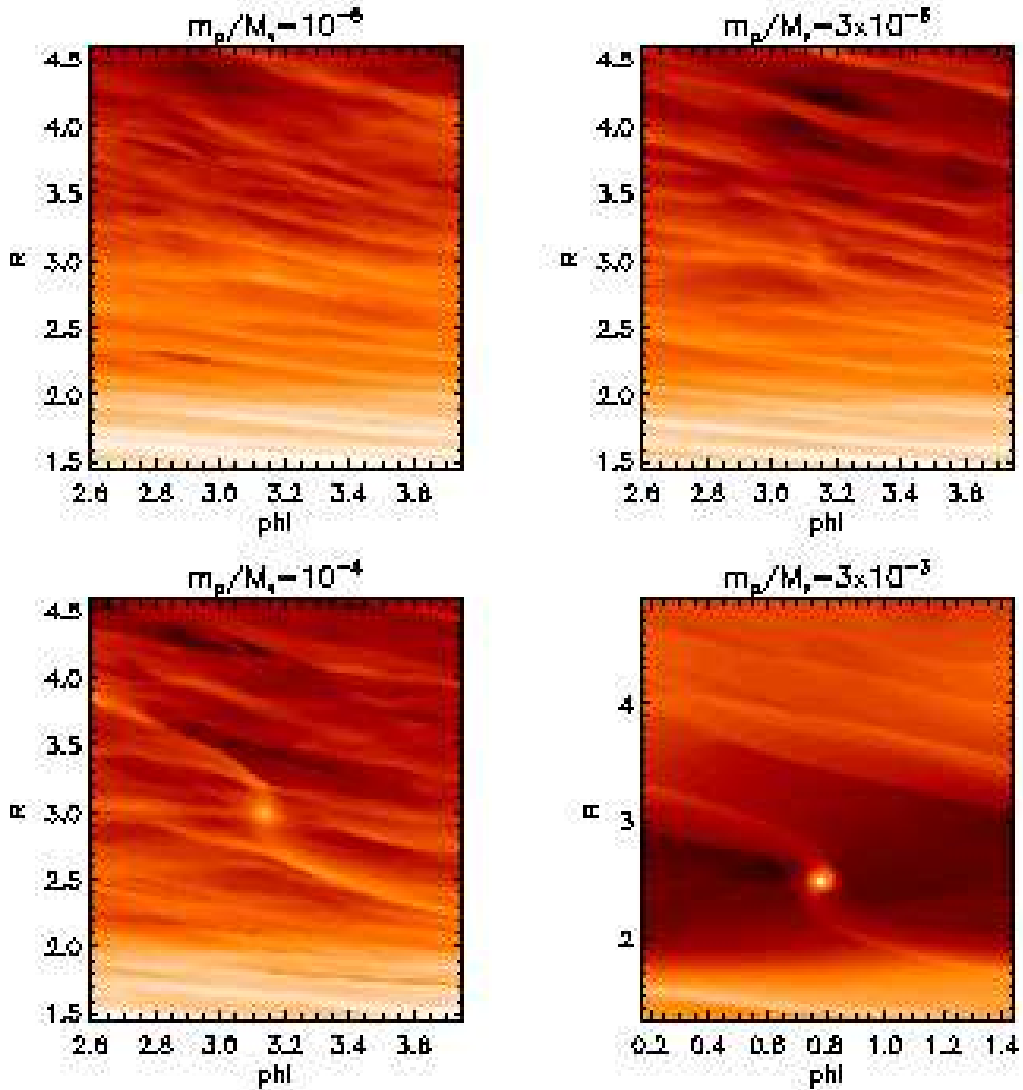


Figure 18. This figure shows the midplane density distribution of runs G1, G2, G3, G5, respectively. The progression of increasing planet mass leads to a clear trend in the disturbance experienced by the disc, with the spiral waves becoming increasingly apparent. Run G5 leads to the formation of a clear gap.

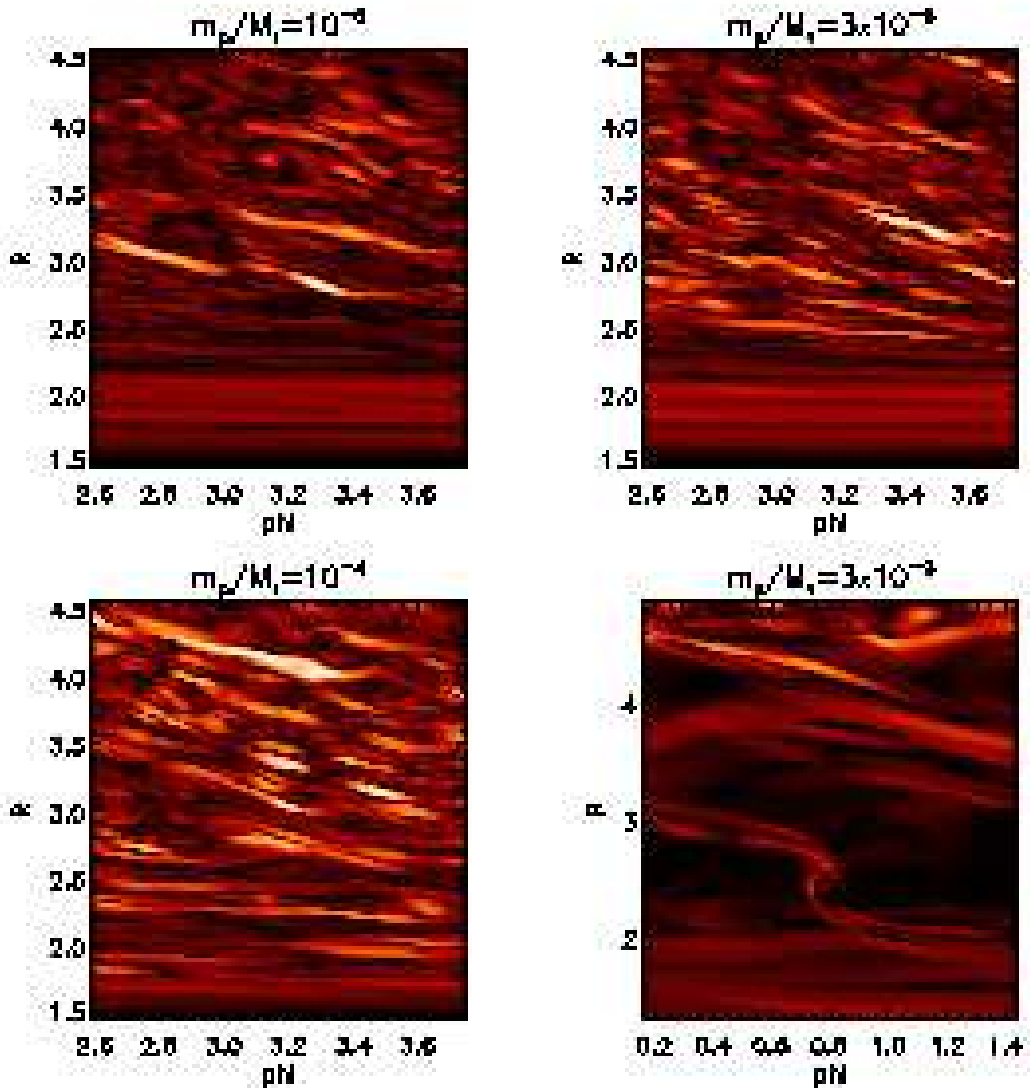


Figure 19. This figure shows the distribution of $|B|^2$ in the disc midplane for the runs G1, G2, G3, G5, respectively. For runs G1, G2, G3 the protoplanet make no discernible perturbation to the magnetic field structure. For run G5 the magnetic field strength is increased in the wakes generated by the planet.

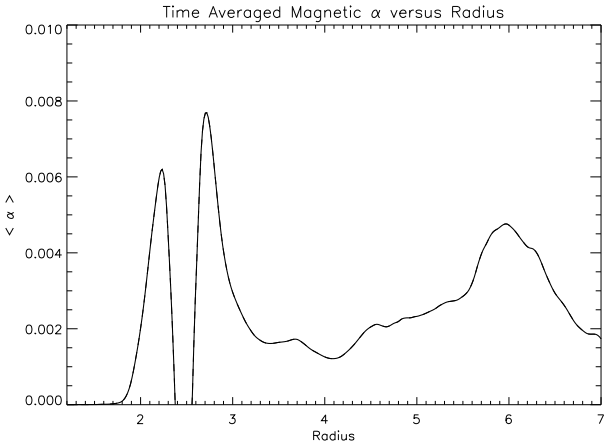


Figure 21. This figure shows a time average of the magnetic contribution to α for run G5. The time averaging occurred for 18 planet orbits. The increase in α in the gap region occurs because of the field concentration in the spiral wakes described in the text.

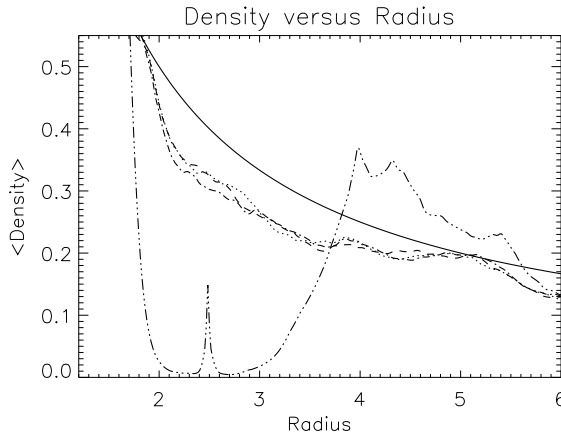


Figure 22. This figure shows the radial density distribution for the runs G1, G2, G3, and G5. The solid line shows the initial $1/r$ density profile of the unperturbed disc. The dotted line corresponds to run G1, the dashed line to G2, and the dash-dotted line to G3. It is clear that there is no gap forming in these cases. The dash-dot-dot-dotted line corresponds to run G5 which shows clear gap formation.

to a final turbulent state. The lower mass protoplanets in runs G1, G2, and G3 have essentially no effect on the underlying density structure, but a deep gap is formed in run G5. This is in line with the expectations discussed in section 2.3 since $(M_p/M_*)/(H/r)^3 < 1$ for G1, G2, and G3, but $(M_p/M_*)/(H/r)^3 \approx 8$ for run G5, and is in very good agreement with the shearing box runs.

We now turn to the question of how the global energetics of the turbulence and the stresses arising from it are affected by the presence of the protoplanets. In the case of the lower mass planets represented by runs G1, G2, and G3 the global magnetic energy of the simulations in units of the volume integrated pressure is essentially unaffected. This is in agreement with the results obtained for a massive 5 Jupiter mass planet embedded in a disc with $H/r = 0.1$ presented in paper II and the shearing box runs. Figure 23

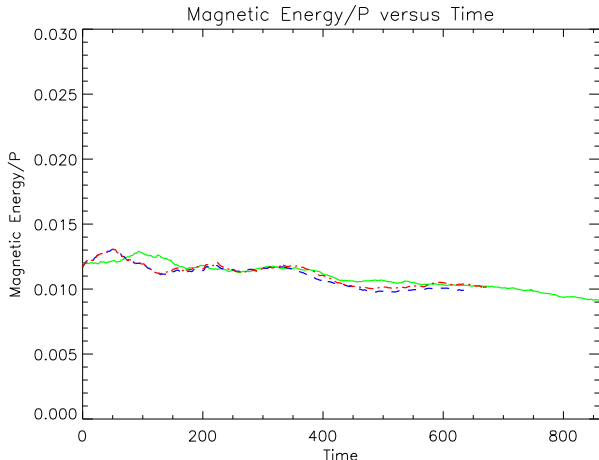


Figure 23. This figure shows the evolution of the magnetic energy in units of the volume integrated pressure for runs G1, G2, and G3. It is clear that the presence of the planets has little effect on the turbulent dynamo as the magnetic energy remains close to its initial value. Variations occur with amplitudes no greater than those associated with the usual turbulent fluctuations.

illustrates this with a plot of $\langle 1/\beta \rangle$ versus time for runs G1, G2, and G3. It is clear that the magnetic energy remains close to its original starting value, with the level of variation no larger than the fluctuations normally associated with the turbulent energy. Simulation G3 was initiated with an underlying disc model that had relaxed for a slightly shorter period of time than models G1 or G2, which were initiated with identical underlying turbulent disc models. Although the qualitative evolution of the global magnetic energy is the same in the three cases, it is also interesting to compare the detailed evolution of $\langle 1/\beta \rangle$ for models G1 and G2. Figure 23 shows that initially the evolution is almost identical. However, after ~ 100 time units they clearly begin to diverge due to the ‘chaotic’ nature of the turbulence, as noted by Winters, Balbus, & Hawley (2003). A similar result is obtained in the shearing box runs. Nonetheless the global properties of the disc models remain similar, even though the local details change. This also has an impact on the way in which the local statistics of the turbulence are affected by the protoplanet, which in turn affects the detailed evolution of the orbit of the planet. These issues are discussed in greater length in the accompanying paper IV.

In the same way that the magnetic energy is largely unaffected by the presence of the low mass protoplanets, the turbulent stresses are also unaffected. This is illustrated by figure 24 which shows the various contributions to α as a function of time for run G2 and should be compared with figure 16. Similar plots are obtained for runs G1 and G3.

The picture is a little different when we consider run G5. The time evolution of $\langle 1/\beta \rangle$ is shown in figure 25, which shows that the evolution of the magnetic energy appears to decrease during the simulation, before reaching a minimum value of $\langle 1/\beta \rangle \approx 0.005$ beyond which it decreases no further. Such a decrease did not occur during the other global runs (G1-G3), or in the calculation of a massive planet in a turbulent disc in paper II. At the present time it is unclear whether the turbulent energy is being affected by the protoplanet in such a manner that the turbulent dynamo is

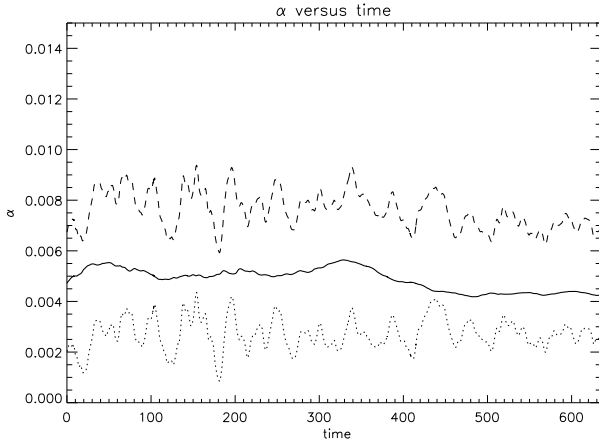


Figure 24. This figure shows the evolution of the stress parameter α for the run G2. The upper line represents the total stress, the middle line the Maxwell stress, and the lowest line the Reynolds stress. The total $\alpha \simeq 7 \times 10^{-3}$.

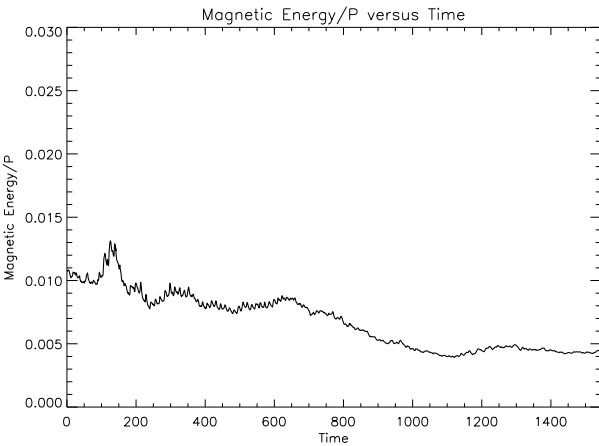


Figure 25. This plot shows the evolution of the magnetic energy, in units of the volume integrated pressure, for run G5. This quantity decreases initially from ~ 0.01 to ~ 0.045 before leveling off.

operating less efficiently due to the ongoing planetary perturbation, or whether the decrease is the result of a large but temporary fluctuation induced by inserting the planet instantaneously in the turbulent disc. The former scenario is conceivable when one considers that the azimuthal domain in run G5 is $\pi/2$ so that the fluid experiences the (strong) perturbation of the planet four times more frequently than it would do in a full 2π disc. Such a strong and frequent perturbation may be able to affect the underlying dynamo in such a way as to reduce the magnetic energy. The shearing box runs in general do not support this picture, but run Bb4 did also show a reduction in magnetic energy once the planet was inserted.

We now consider the impact of the embedded protoplanets on the velocity field of the disc, and specifically the point at which the horseshoe orbits are clearly established. Figure 26 shows the fluid trajectories for two runs. The upper panel corresponds to a global calculation in which a protoplanet with $M_p/M_* = 10^{-4}$ is embedded in a laminar

disc (i.e. the protoplanet is the same as that in run G3). Close inspection of this plot shows that the horseshoe trajectories are established in this case. The lower panel shows the velocity field for run G3, where it is apparent that the horseshoe trajectories are disrupted by the turbulent velocity field. In other words the turbulence determines the fluid trajectories in this case, and the gravitational potential due to the planet is unable to establish the horseshoe orbits in the coorbital zone that are obtained in a laminar disc model.

Figure 27 shows the fluid trajectories for run G5. The horseshoe orbits in this case are very clearly defined, in agreement with the shearing box run Ba4. In this model the circulating region around the planet in the Hill sphere is also clearly visible. The effect of the turbulence on the velocity field in such a strongly perturbed model is essentially indiscernible in the near vicinity of the planet.

In paper II the circulating region around the protoplanet in the Hill sphere was found to be disrupted, and this was tentatively ascribed to magnetic braking caused by magnetic linkage between the circumplanetary disc and the protostellar disc (see also figure 20). A similar situation was also found in the shearing box runs Ba3 and Ba4, where the usual circulating region in the Hill sphere was found to be absent. In these runs the gravitational softening adopted was $b \simeq 0.3H$, which is quite large, and results in gas that accretes into the Hill sphere forming an ‘atmosphere’ that is largely pressure supported but with some angular momentum. In this case the removal of angular momentum will lead to a reduction of the spin of the atmosphere, as observed. The softening used in run G5 was $b = 0.1H$, and so the formation of a rotationally supported circumplanetary disc is more pronounced. The removal of angular momentum in this case may allow further gas accretion into the Hill sphere without a modification of the rotational profile. The issue of magnetic braking of a rotationally supported circumplanetary disc will be the subject of a future publication.

6 DISCUSSION

In this paper we have performed both global cylindrical disc simulations and local shearing box simulations of protoplanets interacting with a disc undergoing MHD turbulence with zero net flux fields. The aim has been to extend the results obtained in a previous paper (paper II) to a wider range of protoplanet masses and conditions of perturbation of the surrounding disc.

Global simulations are naturally more realistic but their computational demands mean that only very few can be carried out. The advantage of local shearing box calculations is that more runs can be done at higher resolution even though larger boxes than are normally considered (e.g. Brandenburg et al. 1995; Hawley et al. 1995) are required in order to adequately contain the response to a perturbing protoplanet.

Another advantage is that for zero net flux fields there exists a natural scaling indicating that results depend only on the parameters $M'_p = M_p R^3 / (M_* H^3)$ and Y/H . Using simple dimensional considerations of the condition for non linear response and balance of viscous and tidal torques we estimated a simple condition for gap formation given by equation 13 in the form $M_p R^3 / (M_* H^3) > \max(C_t, 0.07(Y/H))$. For the conditions of the local and

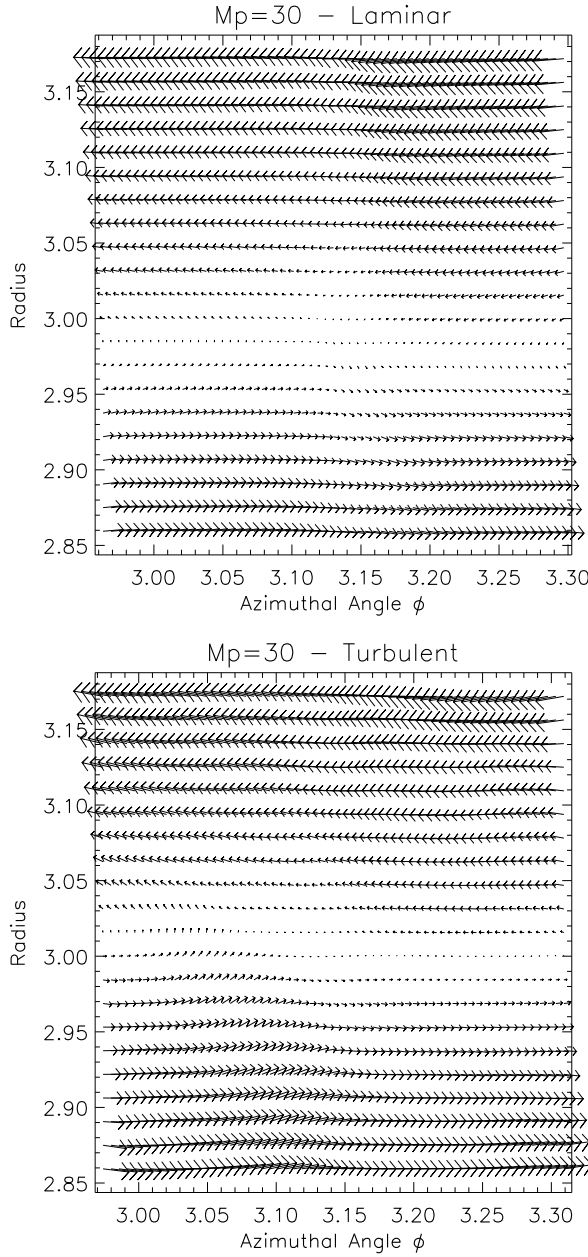


Figure 26. This plot shows the fluid trajectories for a laminar run with $M_p/M_* = 10^{-4}$ (upper panel) and for run G3 (lower panel). The usual horseshoe orbits can be seen in the upper panel, but the turbulence appears to dominate the trajectories in the lower panel. Note that the protoplanet is located at $(r_p, \phi_p) = (\sim 3, \pi)$. We note that plotting the velocity field for run G3 at different times leads to significant variation in the appearance of the velocity field because of the turbulence, but that the flow morphology in the laminar case is essentially independent of time once established.

global simulations ($Y = \pi R$) we have performed both here and in paper II, this always results in a condition that $M_p R^3 / (M_* H^3)$ exceed a number of order unity (i.e. the thermal condition mentioned by Lin & Papaloizou 1993).

The pattern of behaviour we have found from our simulations is the same for both local and global simulations (which show excellent agreement in the results obtained

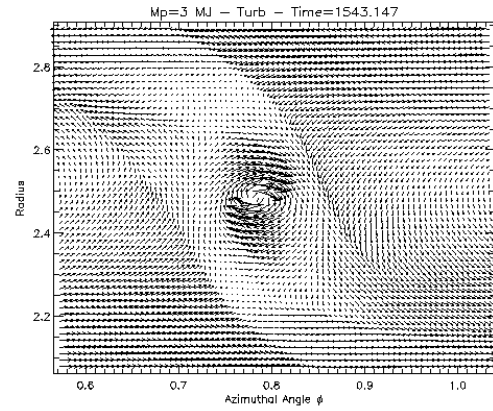


Figure 27. This plot shows the fluid trajectories in the vicinity of the protoplanet for run G5. The horseshoe orbits are clearly visible, as is the circulating region within the Hill sphere.

for the local interaction between protoplanet and turbulent disc) and it agrees with the notion described above. As $M_p R^3 / (M_* H^3)$ is increased to ~ 0.1 the presence of the protoplanet is first manifest with the appearance of the well known trailing wake that can be identified with a characteristic ray emanating from the protoplanet. This wake appears to be well defined even though its form may vary erratically due to the turbulent fluctuations. At this stage the magnetic field in the disc is relatively undisturbed by the planet, and the usual horseshoe orbits in the coorbital region are poorly defined because the fluid trajectories are still dominated by the turbulence.

When $M_p R^3 / (M_* H^3)$ exceeds a number around unity a gap starts to develop inside which the magnetic energy density is on average less than that in the rest of the fluid. However, in the gap region it becomes concentrated in the high density wakes that are generated by the protoplanet. At this point the horseshoe orbits in the coorbital zone become apparent as the gravity of the protoplanet dominates the turbulence. A region in which fluid circulates about the protoplanet may be formed in some cases and this may contain a magnetic field that circulates about the protoplanet and links to the wakes leading to the possibility of magnetic breaking of the protoplanetary disc. In this situation the two sides of the disc tend to separate as the gap forms, signaling the onset of type II migration (eg. Ward 1997).

The nature of the migration induced by disc interactions is of key importance during the later stages of planet

formation. This has yet to be considered for a disc with MHD turbulence for low mass embedded protoplanets. The simulation presented in paper II indicates that migration at the expected rate occurs when a gap is fully formed in a turbulent disc, in agreement with type II migration theory. We comment here that the migration rate induced by the interaction is a complex issue on account of the strong turbulent fluctuations, especially for embedded protoplanets. This issue is examined in a companion paper (paper IV).

6.1 Acknowledgements

The computations reported here were performed using the UK Astrophysical Fluids Facility (UKAFF).

REFERENCES

Armitage, P. J., 1998, *ApJ*, 501, L189
 Armitage, P.J., 2002, *MNRAS*, 330, 895
 Balbus, S. A., Hawley, J. F., 1991, *ApJ*, 376, 214
 Bodenheimer, P., Pollack, J.B., 1986, *Icarus*, 67, 391
 Boss, A.P., 2001, *ApJ*, 563, 367
 Brandenburg, A., Nordlund, Å., Stein, R. F., Torkelsson, U., 1995, *ApJ*, 446, 741
 Bryden, G., Chen, X., Lin, D. N. C., Nelson, R. P., Papaloizou, J. C. B., 1999, *ApJ*, 514, 344
 Courant, R., Hilbert, D., *Methods of Mathematical Physics*, Vol. II, John Wiley and Sons, New York, 1962
 D'Angelo, G., Henning, T., Kley, W., 2002, *A&A*, 385, 647
 Goldreich, P., Lynden-Bell, D., 1965, *MNRAS*, 130, 125
 Goldreich, P., Tremaine, S., 1979, *ApJ*, 233, 857
 Hawley, J. F., Gammie, C. F., Balbus, S. A., 1995, *ApJ*, 440, 742
 Hawley, J. F., Stone, J. M., 1995, *Computer Physics Communications*, 89, 127
 Hawley, J. F., Gammie, C. F., Balbus, S. A., 1996, *ApJ*, 464, 690
 Hawley, J. F., 2000, *ApJ*, 528, 462
 Hawley, J. F., 2001, *ApJ*, 554, 534
 Kley, W., 1999, *MNRAS*, 303, 696
 Korycansky, D.G., Papaloizou, J.C.B., 1996, *ApJ*, 105, 181
 Lin, D.N.C., Papaloizou, J.C.B., 1993, *Protostars and Planets III*, p. 749-835
 Lubow, S.H., Seibert, M., Artymowicz, P., 1999, *ApJ*, 526, 1001
 Marcy, G. W., Cochran, W. D., Mayor, M., 2000, *Protostars and Planets IV* (Book - Tucson: University of Arizona Press; eds Mannings, V., Boss, A.P., Russell, S. S.), p. 1285
 Mayor, M., Queloz, D., 1995, *Nature*, 378, 355
 Nelson, R. P., Papaloizou, J. C. B., Masset, F., Kley, W., 2000, *MNRAS*, 318, 18
 Nelson, R.P., Papaloizou, J.C.B., 2003a, *MNRAS*, 339, 993 – Paper II
 Nelson, R.P., Papaloizou, J.C.B., 2003b, *MNRAS*, submitted – Paper IV
 Papaloizou, J.C.B, Lin, D.N.C., 1984, *ApJ*, 285, 818
 Papaloizou, J.C.B., Nelson, R.P., 2003, *MNRAS*, 339, 983 – Paper I
 Pollack, J.B., Hubickyj, O., Bodenheimer, P., Lissauer, J.J., Podolak, M., Greenzweig, Y., 1996, *Icarus*, 124, 62
 Shakura, N. I., Sunyaev, R. A., 1973, *A&A*, 24, 337
 Steinacker, A., Papaloizou, J.C.B., 2002, *ApJ*, 571, 413
 Van Leer, B., 1977, *J. Comp. Phys.*, 23, 276
 Vogt, S. S., Butler, R. P., Marcy, G. W.; Fischer, D. A.; Pourbaix, D., Apps, K., Laughlin, G., 2002, *ApJ*, 568, 352
 Ward, W.R., 1997, *Icarus*, 126, 261
 Winters, W., Balbus, S., Hawley, J., 2003, *MNRAS*, 340, 519
 Whitham, G.B., 1999, 'Linear and Non Linear Waves', Wiley-Interscience
 Ziegler, U., Rüdiger, G., 2000, *A&A*, 356, 1141